

Probing large-scale structures with the 2-point function and the power spectrum: insights into cosmic clustering evolution

Camila Franco,* Felipe Avila, and Armando Bernui
*Observatório Nacional, Rua General José Cristino, 77,
São Cristóvão, 20921-400, Rio de Janeiro, RJ, Brazil*

(Dated: February 5, 2025)

Understanding the large-scale structure of the Universe requires analysis of cosmic clustering and its evolution over time. In this work, we investigate the clustering properties of SDSS blue galaxies, which are excellent tracers of dark matter, along two distinct epochs of the Universe, utilizing estimators like the 2-point angular correlation function (2PACF), the angular power spectra, among others. Considering a model-independent approach, we perform analyses in two disjoint redshift shells, $0 \leq z < 0.06$ and $0.06 \leq z < 0.12$, to investigate the distribution of large cosmic structures. Using Bayesian inference methods, we constrain the parameter that quantifies the galaxy clustering in the 2PACF, enabling us to perform comparisons among different regions on the sky and between different epochs in the Universe regarding the gravitational action on matter structures. Our analyses complement previous efforts to map large-scale structures in the Local Universe. In addition, this study reveals differences regarding the clustering of large cosmic structures comparing two epochs of the Universe, analyses done with diverse estimators. Results reveal, clearly, distinct evolutionary signatures between the two redshift shells. Moreover, we had the opportunity to test the concordance cosmological model under extreme conditions in the highly non-linear Local Universe, computing the amplitude of the angular power spectrum at very small scales. Ultimately, all our analyses serve as a set of consistency tests of the concordance cosmological model, the Λ CDM.

Keywords: large-scale structure of Universe – cosmology: observations

I. INTRODUCTION

The Universe is plenty of complex large structures whose features are unnoticed, in principle, just observing the mapped cosmic objects on the sky (2-dimensional, 2D, projected data) or its distribution in redshift space (Hoffman et al. 2017, Valade et al. 2024). The most interesting features come from a collective evolutionary phenomenon that is predominant throughout the history of the Universe: matter clustering. Revealing it means describing, at the same time, the growth of cosmic structures (from primordial over-densities) and the growth of voids (from primordial under-densities). With the advent of large and deep astronomical surveys, such structures in the Local Universe are now being revealed and studied (Courtois et al. 2012, 2013, 2025, Hoffman et al. 2017, Lopes et al. 2024), although they were predicted in cosmological simulations two decades ago (Pillepich et al. 2018, Schaye et al. 2015, Springel et al. 2005).

In fact, the observed distribution of galaxies in deep surveys presents an intricate network of structures, like filaments, walls, clusters, and voids, forming what has been called the cosmic web, whose description provides crucial insights into the structure and dynamics of the Universe. Filaments are large-scale, thread-like structures in the cosmic web, formed by concentrations of galaxies and dark matter (Bond et al. 1996, Holm-Hansen et al. 2025, Sarkar & Pandey 2025, Sousbie 2011); walls are

vast, sheet-like structures in the cosmic web made up superclusters of galaxies and dark matter (Einasto et al. 2011, Gavazzi et al. 2010, Ramella et al. 1992); clusters and superclusters are dense groupings of galaxies held together by gravity, often containing hundreds to thousands of galaxies, as well as hot gas and dark matter (Gunn & Gott 1972, Press & Schechter 1974, Springel et al. 2005, White & Frenk 1991); voids, instead, are vast and empty regions in the Universe with very few galaxies or matter (Pan et al. 2012, Sheth & van de Weygaert 2004, Tully et al. 2008).

Tomographic analyses in redshift bins can help to comprehend the clustering evolution of cosmic structures (Asorey et al. 2012, Budavári et al. 2003, Donoso et al. 2014, Marques & Bernui 2020, Papovich 2008, Sawangwit et al. 2011). For this, we study clustering properties of galaxies on two disjoint redshift bins using model-independent statistical tools. Our main objectives are: (i) to complement the analyses reported in the literature mapping the cosmic structures at large scales in the Local Universe, revealing large over-dense regions with highly clustered matter and under-dense regions almost void of galaxies (Courtois et al. 2012, Cybulski et al. 2014, Kitaura et al. 2012, Nuza et al. 2014, Pomarède et al. 2013); (ii) to reveal differences regarding the clustering of large cosmic structures comparing two, close but different, epochs in the Universe evolution (Franco et al. 2024, Marques & Bernui 2020); (iii) to test the concordance cosmological model under extreme conditions in the highly non-linear Local Universe, $z \simeq 0$, quantifying the amplitude of the angular power spectrum at very small scales (Franco et al. 2025, Wu & Xia 2025); and, (iv) to perform statistical isotropy examination of the

* camilaf franco@on.br

Local Universe in both redshift bins (Alonso et al. 2015, Novaes et al. 2018).

This work is organized as follows: Section II describes the observational data used in our analyses. In Section III, we outline the theoretical framework of the 2PACF, the covariance matrix, the angular power spectrum, and the role of the parameters involved in this study, along with the methodology for Bayesian parameter inference. The results and discussions are presented in Section IV. Finally, conclusions are provided in Section V.

II. SLOAN DIGITAL SKY SURVEY DATA

Our analyses are carried out using star-forming blue galaxies from the Sloan Digital Sky Survey (SDSS; York et al. 2000) selected through the colour-colour diagram, following the procedure described in Avila et al. (2019). The objects were made available in the twelfth data release (DR12) of SDSS (Alam et al. 2015); the sky footprint of these data is shown in Figure 1.

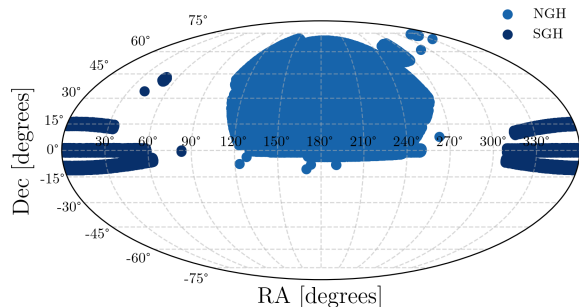


FIG. 1. SDSS footprint in equatorial coordinates. The Northern Galactic Hemisphere (NGH), shown in blue, is the central region of the projection, while the Southern Galactic Hemisphere (SGH), in dark blue, is located at the edges. Both regions have irregular boundaries, with the NGH exhibiting higher density of observations compared to the SGH.

Blue galaxies are predominantly spiral and are observed also in low-density environments, such as cosmic voids (Hoyle et al. 2012, Schneider 2006). These galaxies are characterized by active star-formation, which give rise to their distinct blue colour, primarily due to the presence of young, massive stars (Mo et al. 2010). They are also less clustered than their red counterparts, a cosmic feature manifested in its bias relative to matter close to 1, i.e., $b \approx 1$, highlighting their distinct evolutionary processes in comparison to galaxies in high-density regions (Dressler 1980, Hoyle et al. 2012, Postman & Geller 1984, Strateva et al. 2001). All these features make blue galaxies highly interesting objects for the type of analyses we aim to conduct and also allow us to compare our results with previous studies, such as those using extragalactic HI sources (Franco et al. 2024, Wu & Xia 2025).

For our directional analyses, many disjoint regions as possible are needed, with similar area, and respecting

the lower limit of the homogeneity scale (Avila et al. 2018, 2019). Therefore, we chose the Northern Galactic Hemisphere (NGH), and our sample was subdivided into 12 regions with $\Delta RA \simeq 40^\circ$ and $\Delta Dec \simeq 16^\circ$, within angular coordinates $117^\circ \leq RA < 237^\circ$ and $0^\circ \leq Dec < 64^\circ$. Figure 2 shows the redshift distribution of our sample compared to the full sample.

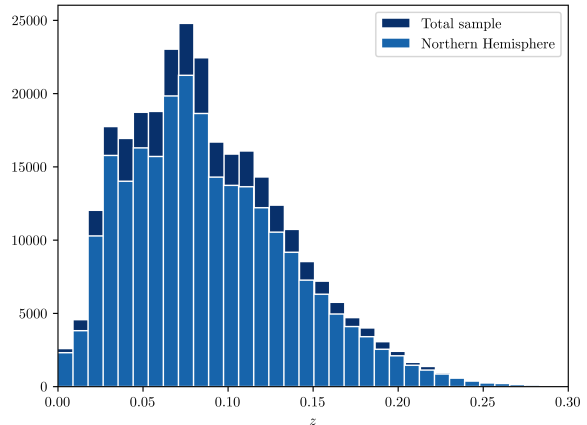


FIG. 2. Redshift distribution of the SDSS blue galaxies selected sample compared to the total sample.

Moreover, in this work we aim to perform model-independent analyses which means that we shall focus on projected 2D data, and in 3D study using the Hubble-Lamaitre law to calculate physical distances with cosmography. For this, we select the SDSS blue galaxies within the redshift $0 \leq z < 0.12$. We perform tomographic analyses in two thin shells, termed Shell 1 ($0 \leq z < 0.06$) and Shell 2 ($0.06 \leq z < 0.12$). The width of the shells is $\delta z = 0.06$. For each shell, the galaxies are projected on the celestial sphere, as seen in Figure 3. The observational features of each region within each shell are listed in Table I. In the end, under these conditions, our selected sample contains 159,207 blue galaxies: 62,495 galaxies in Shell 1 and 96,712 galaxies in Shell 2.

III. METHODOLOGY

In this section, we outline the methodology used to study the distribution of blue galaxies in the SDSS data. It is worth mentioning that our study is based on the angular positions of the galaxies and in their spectroscopic redshifts (that one can use when applying cosmography), ensuring a model-independent approach. However, to establish the significance of our results one needs to perform comparisons with the outcomes expected in the concordance cosmological model, Λ CDM, and for this we use a large set of mocks, data produced assuming a fiducial cosmology.

TABLE I. Features of the 12 regions of the Shell 1 ($0 \leq z < 0.06$) and Shell 2 ($0.06 \leq z < 0.12$). The uncertainties in the number density, n , were calculated using $\sigma_{n_i} = \sqrt{N_i}/\text{area}_i$, where N_i is the number of blue galaxies in area_i . The total volumes of Shells 1 and 2 are, respectively, $V_1 = 1.1 \times 10^{-4} \text{Gpc}^3$ and $V_2 = 7.3 \times 10^{-3} \text{Gpc}^3$.

	area [deg ²]	Shell 1		Shell 2	
		galaxies	n [deg ⁻²]	galaxies	n [deg ⁻²]
Area 1	544	3,154	5.80 ± 0.10	3,924	7.21 ± 0.12
Area 2	640	4,975	7.77 ± 0.11	6,515	10.18 ± 0.13
Area 3	640	5,611	8.77 ± 0.12	8,614	13.46 ± 0.15
Area 4	512	4,292	8.38 ± 0.13	8,171	15.96 ± 0.18
Area 5	640	4,292	6.71 ± 0.10	5,921	9.25 ± 0.12
Area 6	640	5,272	8.24 ± 0.11	7,426	11.60 ± 0.13
Area 7	640	7,233	11.30 ± 0.13	9,029	14.11 ± 0.15
Area 8	640	6,170	9.64 ± 0.12	12,144	18.98 ± 0.17
Area 9	584	2,736	4.68 ± 0.09	5,403	9.25 ± 0.13
Area 10	640	4,390	6.86 ± 0.10	7,088	11.08 ± 0.13
Area 11	640	6,342	9.91 ± 0.12	11,223	17.54 ± 0.17
Area 12	640	8,028	12.54 ± 0.14	11,254	17.58 ± 0.17

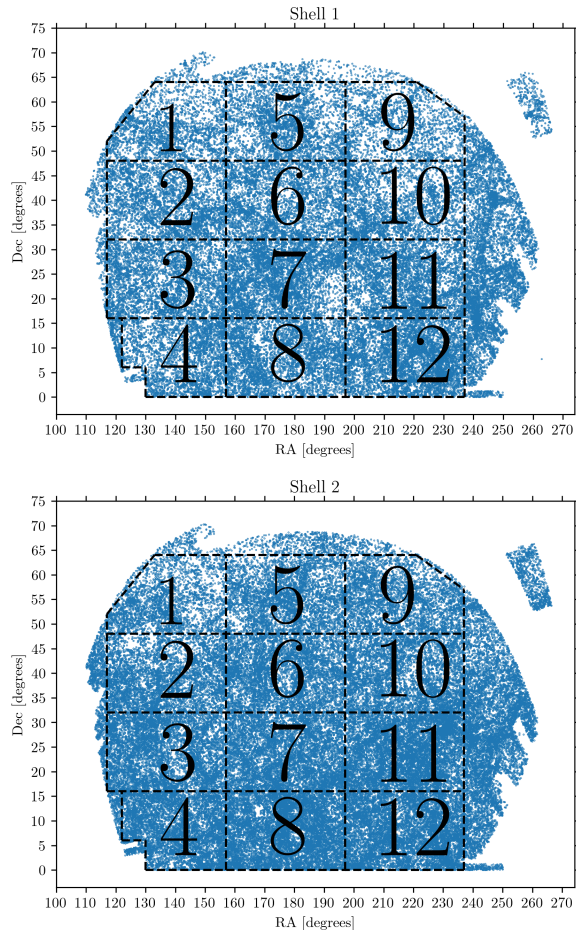


FIG. 3. Footprint of the selected sample, located in the NGH. We divided each shell into 12 regions. **Upper panel:** Shell 1 ($0 \leq z < 0.06$) contains 62,495 galaxies; **Bottom panel:** Shell 2 ($0.06 \leq z < 0.12$) contains 96,712 galaxies.

A. 2-point angular correlation function (2PACF)

The spatial distribution of objects can be effectively characterized using the 2-point angular correlation function (2PACF), that has become a cornerstone in observational cosmology for analysing large-scale structures. This powerful statistical tool quantifies the excess probability of finding two objects separated by a given angular distance θ compared to a random distribution. Several estimators have been proposed in the literature for measuring the 2PACF (Davis & Peebles 1983, Hamilton 1993, Hewett 1982, Peebles & Hauser 1974). Among these, the Landy-Szalay (LS; Landy & Szalay 1993) estimator has proven to be the most robust for count-count correlations, and it is defined as

$$\omega(\theta) = \frac{DD(\theta) - 2DR(\theta) + RR(\theta)}{RR(\theta)}, \quad (1)$$

where $DD(\theta)$ is the number of galaxy pairs in the sample data with angular separation θ , normalized by the total number of pairs; $RR(\theta)$ is a similar quantity, but for the pairs in a random sample; and $DR(\theta)$ corresponds to a cross-correlation between a data object and a random object. The angular separation between pairs is calculated using the trigonometric relationship

$$\theta_{ij} = \cos^{-1}[\sin(\delta_i)\sin(\delta_j) + \cos(\delta_i)\cos(\delta_j)\cos(\alpha_i - \alpha_j)], \quad (2)$$

where α_i , α_j and δ_i , δ_j are the right ascension and the declination, respectively, of the galaxies i and j .

To measure the 2PACF, we used the public code TREECORR¹ (Jarvis 2015), applying 22 linearly spaced bins within the angular range $[\theta_{\min}, \theta_{\max}] = [0.001^\circ, 25^\circ]$

¹ https://rmjarvis.github.io/TreeCorr/_build/html/index.html

for the large-angle scenario. Considering the small-angle scenario, we used 12 logarithmically spaced bins within the angular range $[\theta_{\min}, \theta_{\max}] = [0.001^\circ, 10^\circ]$. A random catalogue was constructed for this purpose, maintaining the same angular footprint as the original region but with a uniform distribution of points and a number density 10 times greater than that of the observed dataset. For further details on random catalogue construction, see, e.g., Keihänen et al. (2019), Wang et al. (2013), de Carvalho et al. (2018).

B. Log-normal simulations

The covariance matrix was used to estimate uncertainties, as it provides reliable error estimates by accounting for correlations between data points. To compute the covariance matrix, we used mock catalogues generated under cosmological conditions consistent with the observational data. We adopted log-normal random field distributions (Coles & Jones 1991), which have been widely used in similar studies (Avila et al. 2024, Franco et al. 2024). For this analysis, we utilized the publicly available code by Agrawal et al. (2017)², which offers a robust way to generate mock catalogues. The input parameters required to create these catalogues, including the cosmological parameters from Planck Collaboration et al. (2020), are detailed in Tables II and III, respectively. Following this approach, 1,000 mock catalogues were generated to ensure statistical reliability. For further details on the pipeline to produce the set of mocks see, e.g., Franco et al. (2024).

TABLE II. Survey configuration used to generate the set of 1,000 log-normal mock catalogues used in our analyses. N_g is the number of galaxies in the box configuration, with dimensions (L_x, L_y, L_z) ; z is the redshift; and b is the bias (Avila et al. 2024).

Survey configuration
$z = 0.08$
$b = 1.1$
$N_g = 5 \times 10^6$
$L_x = 750 \text{ Mpc } h^{-1}$
$L_y = 1,200 \text{ Mpc } h^{-1}$
$L_z = 750 \text{ Mpc } h^{-1}$

TABLE III. Cosmological parameters from Planck Collaboration et al. (2020).

Cosmological parameters
$\Omega_b h^2 = 0.02236$
$\Omega_c h^2 = 0.1202$
$\ln(10A_s) = 3.045$
$n_s = 0.9649$
$\Sigma m_\nu = 0.06 \text{ eV}$
$h = 0.6727$

The covariance matrix was calculated using the following expression,

$$\text{Cov}_{ij} = \frac{1}{N} \sum_{k=1}^N [\omega_k(\theta_i) - \bar{\omega}_k(\theta_i)][\omega_k(\theta_j) - \bar{\omega}_k(\theta_j)], \quad (3)$$

where the indices $i, j = 1, 2, \dots, N_b$ represent each bin θ_i ; ω_k is the 2PACF for the k -th mock ($k = 1, 2, \dots, N$); $\bar{\omega}(\theta_i)$ and $\bar{\omega}(\theta_j)$ are the mean value at the bin i and j , respectively. This approach allows for a more precise quantification of uncertainties, ensuring the robustness of the results presented in this work.

C. Angular Power Spectrum

Matter fluctuations can be described using the 2-point correlation function, either in Fourier space through the power spectrum, $P(k)$, where k is the magnitude of the wave vector, or in real space (configuration space) via the correlation function, $\xi(r)$, where r represents the physical separation between two objects (Peebles 1980). These two approaches are Fourier transform pairs, with k and r being inversely proportional ($k \sim 1/r$). The choice between these methods for studying large-scale structures depends on the specific goals of the analysis, as each may be more suitable for different applications. Currently, in collaborations such as DESI, both estimators $\xi(r)$ and $P(k)$ are often presented to provide complementary insights (DESI Collaboration et al. 2024).

Both 2-point correlation functions, $P(k)$ and $\xi(r)$, can be studied from data projected onto the celestial sphere. In the previous section, we saw the angular correlation function, $\omega(\theta)$, which is the projection of $\xi(r)$. For the projection of $P(k)$, we first need to define the matter fluctuation in the sphere, at a given epoch z_i ,

$$\delta(\theta, \phi) \equiv \frac{\rho(\theta, \phi) - \bar{\rho}}{\bar{\rho}}, \quad (4)$$

where $\bar{\rho}$ is the average number density over the sky at the epoch z_i . Note that we avoid using distances so as not to use a cosmological model in their determination. Then, having defined the fluctuation of matter in the celestial sphere, the decomposition into spherical harmonics is applied (for theoretical methodology and its application, see Ando et al. (2018), Fang et al. (2020), Leistedt et al.

² https://bitbucket.org/komatsu5147/lognormal_galaxies/src/master/

(2013), Peebles (1980), Tegmark et al. (2002), Thomas et al. (2011)),

$$\delta(\theta, \phi) = \sum_{\ell=0}^{\infty} \sum_{m=-\ell}^{\ell} a_{\ell,m} Y_{\ell,m}(\theta, \phi), \quad (5)$$

where the power spectrum, C_{ℓ} , is obtained from the variance of the coefficients $a_{\ell,m}$,

$$C_{\ell} = \langle |a_{\ell,m}|^2 \rangle. \quad (6)$$

The multipole moment, ℓ , is related to the angular scale, θ , approximately as $\ell \sim 180^\circ/\theta$, where θ is measured in degrees. Since we will be using the public code CCL³ (Chisari et al. 2019) to obtain the theoretical curve of C_{ℓ} , we will use their notation to define C_{ℓ} in function of the matter power spectrum. For two tracers, a and b , the angular power spectrum can be written as

$$C_{\ell}^{ab} = 4\pi \int_0^{\infty} \frac{dk}{k} \mathcal{P}_{\Phi}(k) \Delta_{\ell}^a(k) \Delta_{\ell}^b(k), \quad (7)$$

where $\mathcal{P}_{\Phi}(k)$ is the dimensionless power spectrum of the primordial curvature perturbations, and $\Delta_{\ell}^a(k)$ and $\Delta_{\ell}^b(k)$ are the transfer functions corresponding to these tracers. In our case, we are dealing with discrete sources, these transfer functions can be calculated as

$$\Delta_{\ell}(k) = \int dz p_z(z) b(z) T_{\delta}(k, z) j_{\ell}[k\chi(z)], \quad (8)$$

where $p_z(z)$ is the normalized distribution of the sources, $b(z)$ is the linear bias, $T_{\delta}(k, z)$ is the matter over-density transfer function, and $j_{\ell}[k\chi(z)]$ is the ℓ -th order spherical Bessel function, for a comoving distance $\chi(z)$. For our purposes, the theoretical curve will be obtained with the linear matter power spectrum for a constant linear bias $b(z) = 1$. In this way, we can interpret the clustering at different scales by comparing it with the distribution of dark matter in a linear perturbation theory.

In real surveys, the sky coverage is not complete, and the observed galaxy distribution is masked by regions where observations are not possible (e.g., due to foreground contamination or survey limitations). This partial sky coverage introduces correlations between different ℓ modes, which must be considered in the analysis. The effect of the survey mask is described by the mixing matrix, $R_{\ell\ell'}$, which convolves the true angular power spectrum with the power spectrum of the mask,

$$C_{\ell}^{\text{obs}} = \sum_{\ell'} R_{\ell\ell'} C_{\ell'}^{\text{true}}. \quad (9)$$

Following Wu & Xia (2025), we use the public code NASTMASTER⁴ (Alonso et al. 2019) to calculate the true angular power spectrum.

D. β parameter estimation

Under the assumptions of isotropy and homogeneity, the expected behaviour of the 2PACF follows a power-law distribution given by (Coil 2013a, Connolly et al. 2002, Kurki-Suonio 2023, Marques & Bernui 2020, Peebles 1993, Totsuji & Kihara 1969)

$$\omega(\theta) = \left(\frac{\theta}{\theta_0} \right)^{-\beta}, \quad (10)$$

where θ_0 and β are parameters related to the transition scale between linear and non-linear regimes, and the slope of the correlation, respectively (Coil 2013b, Connolly et al. 2002, Marques & Bernui 2020, Peebles 1993).

To estimate the parameters θ_0 and β , we adopted a Bayesian inference approach using Markov Chain Monte Carlo (MCMC) methods. This iterative process allows for an efficient exploration of the parameter space, leading to more reliable estimates of the posterior distributions (Trotta 2017). For this analysis, we utilized the publicly available EMCEE⁵ code (Foreman-Mackey et al. 2013).

Given a model characterized by a set of parameters Θ and a dataset \mathbf{D} , Bayesian inference computes the posterior probability distribution, $P(\Theta|\mathbf{D})$, following Bayes' theorem,

$$P(\Theta|\mathbf{D}) = \frac{P(\mathbf{D}|\Theta)P(\Theta)}{P(\mathbf{D})}. \quad (11)$$

The logarithm of the scaled posterior distribution is expressed as

$$\log P(\Theta|\mathbf{D}) \propto \log P(\mathbf{D}|\Theta) + \log P(\Theta), \quad (12)$$

where the likelihood can be written as

$$\log P(\mathbf{D}|\Theta) \propto -\frac{1}{2}\chi^2, \quad (13)$$

and, in this work,

$$\chi^2 = \sum_{i,j} [\omega(\theta_i) - \omega^{\text{PL}}(\theta_i; \theta_0, \beta)] \times C_{i,j}^{-1}(\theta_i, \theta_j) \times [\omega(\theta_j) - \omega^{\text{PL}}(\theta_j; \theta_0, \beta)], \quad (14)$$

where $\omega(\theta_i)$ represents the measured correlation function, $\omega^{\text{PL}}(\theta_i; \theta_0, \beta)$ is the model prediction with power law parameters θ_0 and β , and $C_{i,j}^{-1}(r_i, r_j)$ is the inverse covariance matrix of the measurements, given by equation (3).

For the MCMC implementation, the prior distributions for θ_0 and β were chosen based on typical values for galaxies (Franco et al. 2024, Wang et al. 2013). The priors used are detailed in Table IV.

³ <https://github.com/LSSTDESC/CCL>

⁴ <https://github.com/LSSTDESC/NaMaster>

⁵ <https://emcee.readthedocs.io/en/stable/>

TABLE IV. Prior ranges for the power-law parameters.

Parameter	Prior distribution
θ_0	[0.01, 0.13]
β	[0.2, 1.0]

The parameter β , in particular, is very useful in our analyses. It not only defines the slope of the correlation function, but also serves as an estimator for quantifying the degree of matter clustering. As discussed in Franco et al. (2024), β provides a robust characterization of the clustering behaviour, offering insights into the underlying cosmological structure.

IV. ANALYSES AND RESULTS

In this section, we present our tomographic analysis in two redshift shells, Shell 1 ($0 \leq z < 0.06$) and Shell 2 ($0.06 \leq z < 0.12$), of blue galaxies. Specifically, our methodology to probe the matter clustering evolution is based on a comparison of the valuable information extracted from both shells using diverse statistical tools.

In fact, a comparison of the results from one shell to the other provides information about the evolutionary process of growth of large structures that host (or are lacking of) blue galaxies. This because the Shell 2 maps the galaxy distribution from a younger epoch compared with the Shell 1, which maps the oldest structures in the Universe, and we intend to capture quantitatively these characteristics in our analyses. This study comprehends the use of diverse tools to study the matter clustering evolution. The statistical estimators employed in the scrutiny of the Local Universe were: the 2PACF (analyses done at small and large angles), the cumulative distribution function (CDF), and the angular power spectra.

A. The 2PACF: small-angle analysis

We start our analyses of the matter clustering studying the 2PACF, at small angles, of the data contained in the 12 Areas selected, in each one of the redshift shells (see Figure 3). For each Area, we calculate the 2PACF, $\omega(\theta)$, for the angular separations $\theta \in [0^\circ, 10^\circ]$. The 2PACF binned data, with their corresponding uncertainties obtained from the mocks, are then used to adjust a best-fit power law, equation (10), using the MCMC approach to find the parameters θ_0 and β . The results for the 12 Areas, in each one of the shells, are displayed in Figures 4 and 5, and summarized in Table V.

The next step is a comparison of the β values from the SDSS data with the set of β values obtained by analysing 1,000 Area-mocks produced according to the fiducial cosmology (see Section III B). The distribution of values obtained for the β parameter, seen in the histograms of Figure 6 provides information regarding the clustering

strength in each shell according to the fiducial cosmology.

The behaviour observed in these distributions, individually and comparatively, is consequence of the growth process of structures. For data from Shell 2, corresponding to a Universe younger than the structures mapped in Shell 1, one observes a bimodality⁶ in the β distribution from the mocks data, suggestive of under-dense regions, as shown in Franco et al. (2024). For the Shell 1, this feature is absent, but the distribution is clearly skewed to the left, perhaps a remnant of the bimodality from the younger epoch.

From the analyses of the 12 Areas in Shell 1, and independently the 12 Areas in Shell 2, summarized in the distributions displayed in Figure 6, they all show consistency with what is expected in the concordance cosmological model, represented by the outcomes from set of mocks. Additionally, because larger values of β means stronger clustered matter one expects that the data in Shell 1 be more clustered than the data in Shell 2; in fact this is corroborated in our analyses of the SDSS blue galaxies and in the data mocks:

$$\beta_1^{\text{SDSS}} = 0.625 \text{ is larger than } \beta_2^{\text{SDSS}} = 0.579; \text{ and } \beta_1^{\text{mocks}} = 0.8 \text{ is larger than } \beta_2^{\text{mocks}} = 0.7.$$

B. The 2PACF: large-angle analysis

The 2PACF analysis at large angles is also valuable to provide insights into the presence and features of large cosmic structures. Similarly, we perform the study of the 12 Areas selected, in each one of the redshift shells (see Figure 3). For each Area, we calculate the 2PACF, $\omega(\theta)$, for the angular separations $\theta \in [0^\circ, 25^\circ]$. The 2PACF binned data, with their corresponding uncertainties obtained from the mocks, are then used to adjust a best-fit power law, equation (10), using the MCMC approach to find the parameters θ_0 and β . The results for the 12 Areas, in each one of the shells, are displayed in Figures 7 and 8 and summarized in Table VI.

The next step is a comparison of the β values from the SDSS data with the set of β values obtaining analysing 1,000 Area-mocks produced according to the fiducial cosmology (see Section III B). The distribution of values obtained for the β parameter, seen in the histograms of Figure 9, and complemented with the Table VI, giving sufficient information for a quantitative comparison both between the Areas in the two shells, as well as the Areas with respect to what is expected in the fiducial cosmology (mocks).

In the large-scale analyses, however, the 2PACF calculated for each Area is more informative than the support offered by the parameters (θ_0, β) . This because one learns

⁶ This bimodality suggests that there exist two populations of blue galaxies: one with small β is localized in under-dense regions like voids and filaments and the other with large β localized in over-dense regions like galaxy groups and clusters

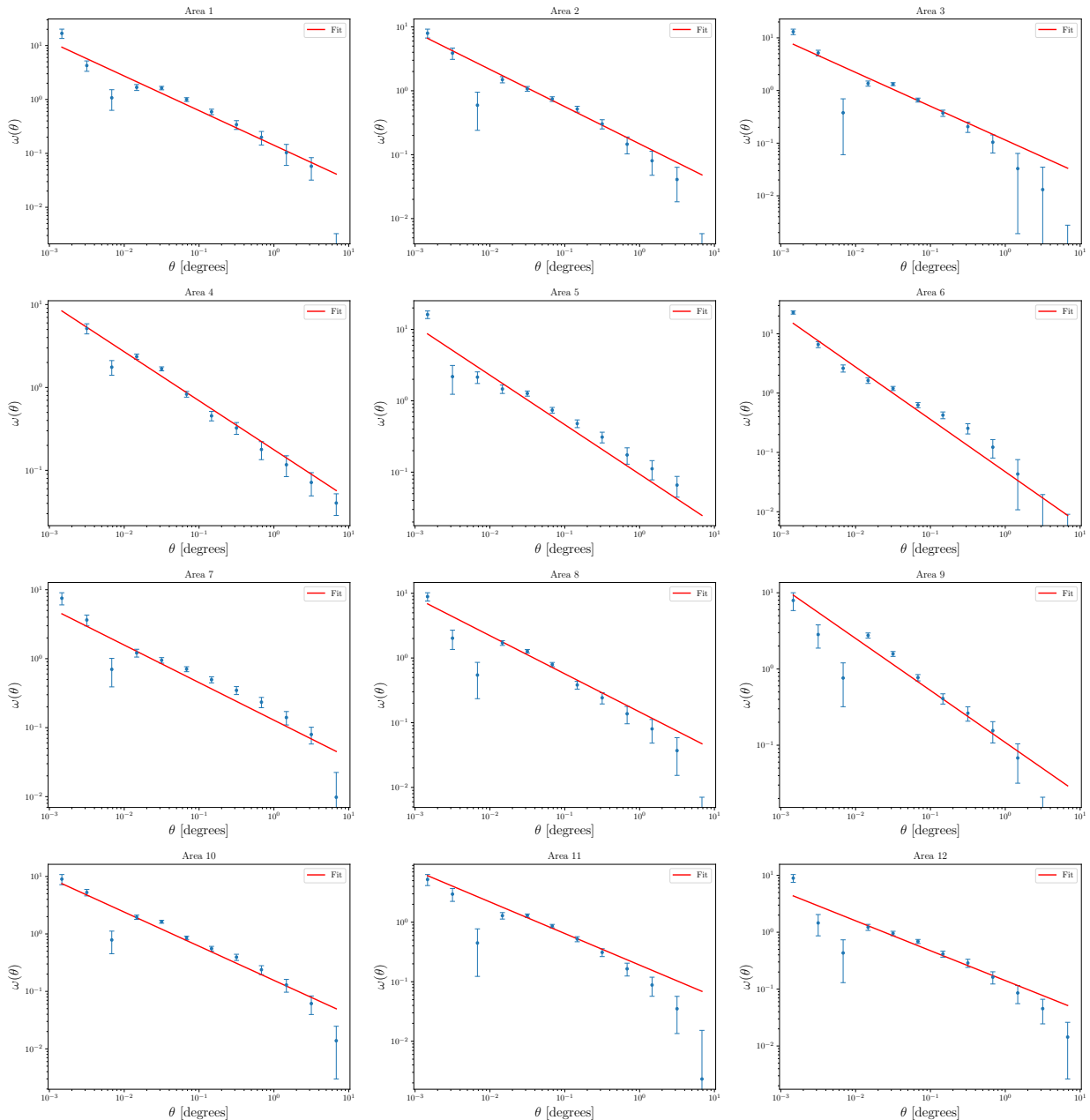


FIG. 4. 2PACF for small-angle analyses in Shell 1. Angular distribution of the 12 regions illustrated in Figure 3 within the angular range $0^\circ < \theta \leq 10^\circ$.

to interpret features observed in the 2PACF as signatures due to the presence of over-dense and under-dense regions in the sample in study, with the obvious caution that this information is relative to the projected data.

The 2PACF, displayed in Figure 7 for the Areas in Shell 1 and Figure 8 for the Areas in Shell 2, show distinctive characteristics of the blue galaxies clustering in each Area and each shell. Regarding the signatures shown by these 2PACF, one clearly distinguish 3 patterns: (i) a flat curve, with small fluctuations around zero (e.g., Areas 6 and 7 from Shell 1); (ii) fluctuation of the data points around zero but with an excess of several points over zero

(e.g., Area 8 from Shell 1 and Shell 2); (iii) fluctuation of the data but with a defect, i.e., a valley, of several data under zero (e.g., Area 5 in Shell 1 and Area 1 in Shell 2).

To better understand what the origin of these signatures could be, we use complementary information provided by wedge plots and CDF plots (for the application of the CDF in this type of analysis see, e.g., Franco et al. (2024)). As observed in Figures 10 and 11, the wedge plots of Area 5 and Area 8, interesting clustered patterns appear. The structures observed in the wedge plot are consequence of the evolutionary process of structures growth along time.

On the other hand, the CDF plots from Areas 1, 5, 6,

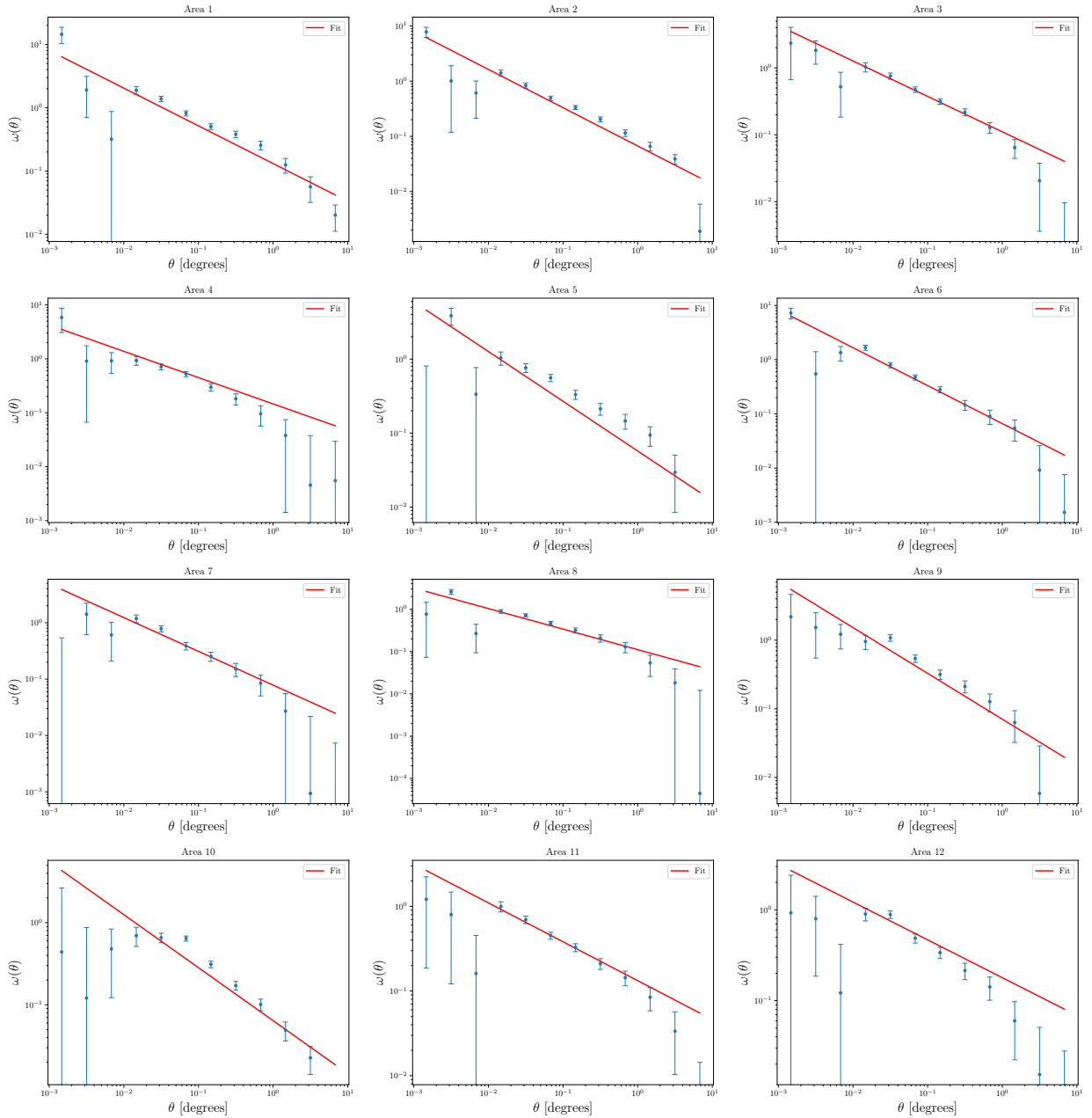


FIG. 5. 2PACF for small-angle analyses in Shell 2. Angular distribution of the 12 regions illustrated in Figure 3 within the angular range $0^\circ < \theta \leq 10^\circ$.

8, both shells, shown in Figure 12 exhibit other type of information. One can observe differences among these CDF plot for different Areas in each shell. But, Areas in a given shell, which means structures with the same age, notably follows the same pattern, namely regions of similar scales with strong clustering followed by regions with lack of galaxies (voids). The presence of these features appears independent of the number galaxies in each Area, N_i , as can be corroborated in the Figures 10 and 11, which presents the wedge plots of Area 5 with $N_5 = 4,292$ and $5,921$, and Area 8 with $N_8 = 6,170$ and $12,144$, for Shell 1 and Shell 2, respectively (see Table I).

As in small scales, on large scales one can also use the β parameter to compare the clustering strength in different Universe epochs, namely in Shell 1 versus in Shell 2. In fact, as expected, Shell 1 exhibits stronger clustering than Shell 2, again confirmed both in the SDSS data in study and in the mock catalogues:

$$\tilde{\beta}_1^{\text{SDSS}} = 1.725 \text{ is larger than } \tilde{\beta}_2^{\text{SDSS}} = 1.700; \text{ and } \tilde{\beta}_1^{\text{mocks}} = 1.2 \text{ is larger than } \tilde{\beta}_2^{\text{mocks}} = 1.1.$$

TABLE V. **Small scales:** Best-fit parameters for the power-law analyses of the 2PACF (Figures 4 and 5): $\omega(\theta) = (\theta/\theta_0)^{-\beta}$. On average, the results for the SDSS blue galaxies are: $\tilde{\theta}_{0,1} = 0.038 \pm 0.009$; $\tilde{\theta}_{0,2} = 0.017 \pm 0.006$; $\tilde{\beta}_1 = 0.625 \pm 0.094$; $\tilde{\beta}_2 = 0.579 \pm 0.096$.

	Shell 1		Shell 2	
	θ_0 [degrees]	β	θ_0 [degrees]	β
Area 1	0.048 ± 0.004	0.642 ± 0.022	0.033 ± 0.004	0.596 ± 0.027
Area 2	0.038 ± 0.003	0.582 ± 0.021	0.020 ± 0.002	0.693 ± 0.024
Area 3	0.034 ± 0.002	0.642 ± 0.026	0.016 ± 0.002	0.529 ± 0.029
Area 4	0.054 ± 0.004	0.590 ± 0.022	0.019 ± 0.002	0.487 ± 0.038
Area 5	0.033 ± 0.002	0.694 ± 0.028	0.014 ± 0.002	0.672 ± 0.038
Area 6	0.031 ± 0.002	0.883 ± 0.035	0.021 ± 0.002	0.700 ± 0.031
Area 7	0.023 ± 0.002	0.545 ± 0.027	0.014 ± 0.002	0.599 ± 0.038
Area 8	0.039 ± 0.003	0.589 ± 0.022	0.011 ± 0.001	0.485 ± 0.025
Area 9	0.039 ± 0.003	0.683 ± 0.025	0.019 ± 0.002	0.667 ± 0.036
Area 10	0.044 ± 0.003	0.594 ± 0.021	0.014 ± 0.002	0.645 ± 0.024
Area 11	0.044 ± 0.003	0.530 ± 0.017	0.012 ± 0.002	0.459 ± 0.028
Area 12	0.024 ± 0.002	0.525 ± 0.023	0.016 ± 0.003	0.416 ± 0.029

TABLE VI. **Large scales:** Best-fit parameters for the power-law analyses of the 2PACF (Figures 7 and 8): $\omega(\theta) = (\theta/\theta_0)^{-\beta}$. On average, the results for the SDSS blue galaxies are: $\tilde{\theta}_{0,1} = 0.232 \pm 0.050$; $\tilde{\theta}_{0,2} = 0.196 \pm 0.045$; $\tilde{\beta}_1 = 1.725 \pm 0.475$; $\tilde{\beta}_2 = 1.700 \pm 0.324$.

	Shell 1		Shell 2	
	θ_0 [degrees]	β	θ_0 [degrees]	β
Area 1	0.22 ± 0.08	1.6 ± 0.4	0.21 ± 0.04	1.3 ± 0.2
Area 2	0.24 ± 0.07	1.8 ± 0.5	0.16 ± 0.03	1.4 ± 0.2
Area 3	0.29 ± 0.19	2.6 ± 2.4	0.18 ± 0.05	1.5 ± 0.3
Area 4	0.19 ± 0.04	1.1 ± 0.1	0.29 ± 0.15	2.3 ± 1.7
Area 5	0.24 ± 0.07	1.7 ± 0.4	0.21 ± 0.08	1.8 ± 0.6
Area 6	0.31 ± 0.13	2.5 ± 1.7	0.23 ± 0.07	1.9 ± 0.6
Area 7	0.25 ± 0.04	1.4 ± 0.2	0.25 ± 0.13	2.2 ± 1.4
Area 8	0.15 ± 0.07	1.4 ± 0.3	0.13 ± 0.07	1.4 ± 0.4
Area 9	0.26 ± 0.17	2.3 ± 1.8	0.20 ± 0.14	2.0 ± 1.3
Area 10	0.24 ± 0.04	1.4 ± 0.2	0.18 ± 0.05	1.7 ± 0.3
Area 11	0.26 ± 0.06	1.7 ± 0.4	0.18 ± 0.06	1.5 ± 0.4
Area 12	0.13 ± 0.05	1.2 ± 0.2	0.13 ± 0.11	1.4 ± 0.7

1. Revealing the signature of galaxy groups and clusters

One efficient way to confirm if galaxies clustered in small or large groups (i.e., galaxy clusters) are leaving a signature in the 2PACF, is by performing small angular shifts in their positions and then redoing the 2PACF to observe whether the signature decreases, disappears or nothing happens. In fact, one observes in the 2PACF of Area 8 a set of lumps and valleys at diverse angular scales, suggestive of (large) groups of galaxies (Einasto 2001), that is, the 2PACF is revealing the presence of various galaxy groups or clusters in that region.

A shuffling procedure is then applied to Area 8, where the new angular coordinates RA and Dec of each blue galaxy are randomly selected from a Gaussian distribution where the mean value is the original coordinate and the standard deviation is 0.5° (this scale corresponds to the double value of θ_0 obtained in Table VI, where for lower scales non-linearities dominate). The panels shown

in Figure 13 presents the result obtained applying this shuffling procedure. If they correspond, indeed, to galaxies concentrated in small groups or galaxy clusters then the shuffling of their angular positions will tend to destroy these features. In Figure 13, we display the results of this shuffling procedure done in both shells of Area 8. The sequence of panels, from left to right, is: (i) the original 2D blue galaxies distribution; (ii) these blue galaxies overlapped with their shuffled distribution; (iii) the 2PACF study for both distributions, i.e., analyses of the original distribution together with that one from the shuffled distribution.

Our conclusion is that, in fact, Area 8 contains large groups of galaxies. But perhaps more importantly, the analysis of the 2PACF of Area 8 clearly illustrates the expected difference between two distinct epochs: the Shell 2 (snapshot of a less evolved Universe) shows less galaxy groups than the Shell 1 (snapshot of a more clustered Universe).

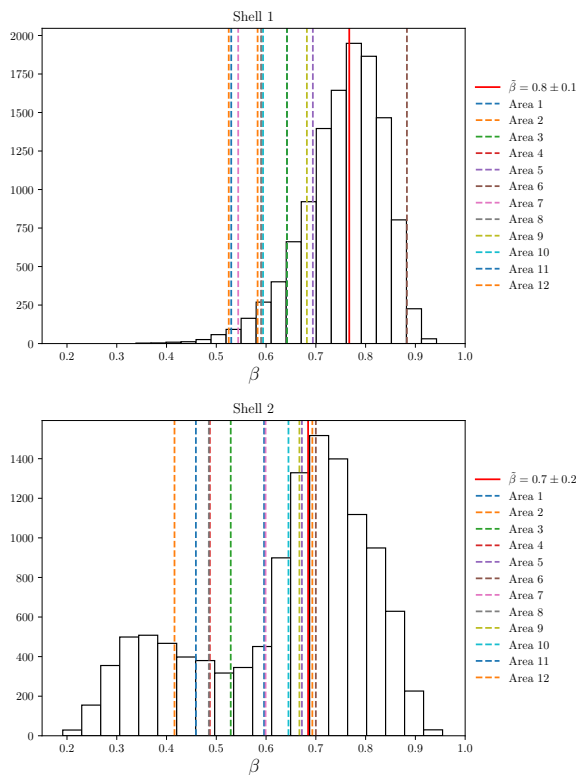


FIG. 6. Small-scales case. **Upper:** Distribution of the best-fit parameters of 1,000 Area-mocks in Shell 1 ($0 \leq z < 0.06$). The median and standard deviation are $\tilde{\beta} = 0.8 \pm 0.1$. **Bottom:** Distribution of the best-fit parameters of 1,000 Area-mocks in Shell 2 ($0.06 \leq z < 0.12$). The median and standard deviation are $\tilde{\beta} = 0.7 \pm 0.2$.

C. Angular Power Spectrum analysis

To compute the angular power spectrum for the selected shells with the SDSS blue galaxies, we use the HEALPIX⁷ pixelation scheme (Górski et al. 2005), provided by the HEALPY⁸ library (Zonca et al. 2019). This tool allows us to construct a fluctuation map and the application of the corresponding mask. Using the fluctuation map and the mask, we calculate the C_ℓ^{true} and estimate the shot noise ($1/\bar{n}$), which is then subtracted to isolate the cosmological signal.

The pixelization scheme requires a choice of pixel sizes related to the N_{side} parameter, which determines the number of pixels on the sphere, given by the relationship

$$N_{\text{pix}} = 12N_{\text{side}}^2. \quad (15)$$

The choice of the pixelization parameter, N_{side} , is crucial for our study of the matter clustering, i.e., over-dense and under-dense regions, through the analysis of the angular

power spectrum. A low N_{side} value may fail to capture the features of the galaxy distribution accurately, while a large N_{side} gives rise to pixels with few galaxies, introducing bias into the estimator. After some tests, we choose $N_{\text{side}} = 64$ for our analyses. In Figure 14, we present the number count maps for the two selected shells. For comparison purposes, the analyses performed with $N_{\text{side}} = 32$ are provided in the Appendix A. In summary, reducing N_{side} from 64 to 32 implies less accuracy at small-scales, losing information on high- ℓ multipoles. However, when comparing the two spectra, no significant differences are observed within the displayed 2σ confidence interval.

The true angular power spectrum, after shot-noise subtraction, for the two shells is presented in Figure 15. The multipole range is $\ell \in [7, 183]$, with a bin size of $\Delta\ell = 11$. The vertical axis is dimensionless, as the maps represent fluctuations. The uncertainties were derived from the standard deviation of the results obtained from 1,000 mock simulations, using the same data methodology applied to the mocks. Similar to what was done with the correlation function, $\omega(\theta)$. From a qualitative perspective, the result aligns with expectations: there is more power at small ℓ , with a decrease in power at large ℓ . Additionally, due to the evolution of the Universe, Shell 1 exhibits more power than Shell 2. We also notice that, because the redshift shells are contiguous, at large scales the power spectra are comparable.

To validate the results of our analyses, a comparison between observation and theory is necessary. In the Λ CDM model, within the theory of linear perturbations, the theoretical curve can be obtained using equation (7). In the linear context, it is expected that the theoretical C_ℓ^{th} is proportional to the observed C_ℓ^{obs} . Since C_ℓ^{th} is proportional to b_0^2 , one can calculate the quantities $\sqrt{C_\ell^{\text{obs}}/C_\ell^{\text{th}}}$, for $\ell \in [7, 183]$. We present the results of this comparison in Figure 16 for both shells. The shaded region represents the propagated error in 1σ . Up to the multipole $\ell = 90$, both curves intersect, with a bias close to 1 within a 2σ confidence interval. However, as expected, for very low multipoles, the measurements show more power than predicted by linear theory. This could suggest that non-linear effects appear for scales $\ell \gtrsim 90$. Another key observation in this figure is that the curve for Shell 2 is closer to the linear theory than that of Shell 1, suggesting that our neighbourhood, $0 \leq z < 0.06$, has more developed structures that contribute to non-linear measurements. This is further illustrated in Figure 17, where the results are compared with the mock simulations. For the entire range of ℓ , the data points for Shell 2 are in excellent agreement with the log-normal simulations. For Shell 1, a discrepancy is noticed for $\ell \gtrsim 90$. We cannot fail to mention that our mocks were generated with a non-linear power spectrum, but for very small scales the non-linear effects observed in our analyses contribute to the increase in power in a way not expected in the simulations (Matthewson & Durrer 2022).

⁷ <https://healpix.sourceforge.io/>

⁸ <https://healpy.readthedocs.io/en/latest/>

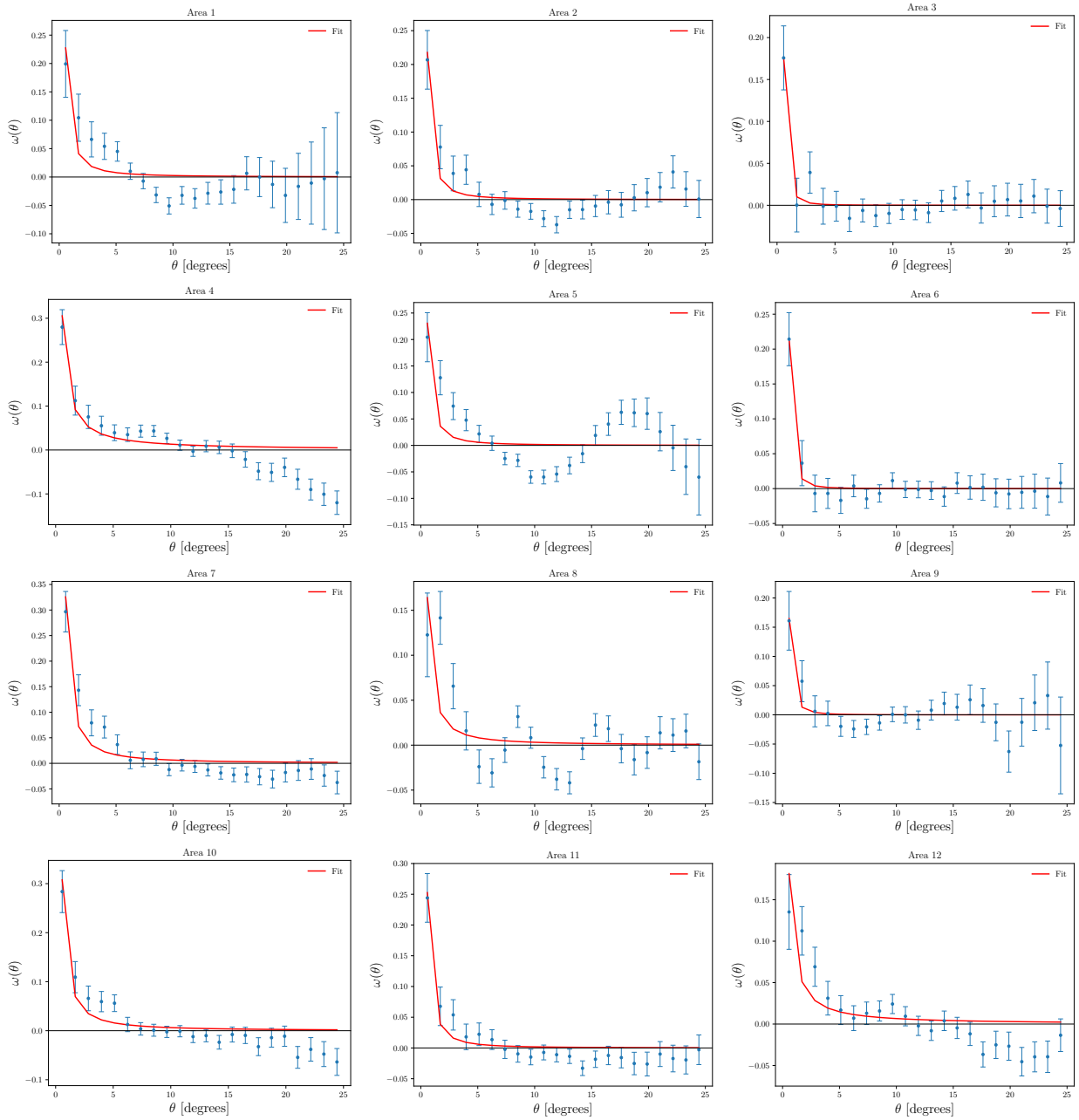


FIG. 7. 2PACF for large-angle analyses in Shell 1. Angular distribution of the 12 regions illustrated in Figure 3 within the angular range $0^\circ < \theta \leq 25^\circ$.

V. CONCLUSIONS AND FINAL REMARKS

We employ the SDSS blue galaxies, excellent tracers of dark matter, to discover clustering properties of the network of cosmic structures, and for this we use various estimators that provide partial, but complementary, insights to solve the big cosmic puzzle.

With the 2PACF, at small and large scales, we have studied quantitatively –through the β parameter– the clustering strengths of the SDSS blue galaxies finding them consistent with the clustering and growth of cos-

mic structures obtained from the analysis of the set of simulated mocks. The clustering is quantified by β , and the values obtained analysing the data make sense when compared with the average from a similar analysis made with the mocks; instead the growth of cosmic structures is confirmed by comparison between the β values in both shells. In fact, the confront of β between different epochs reflects the gravitational process of gravitational instability shaping the matter distribution, with Shell 1 showing more evolved and clustered structures compared to Shell 2, which maps a (slightly) younger epoch of the Universe.

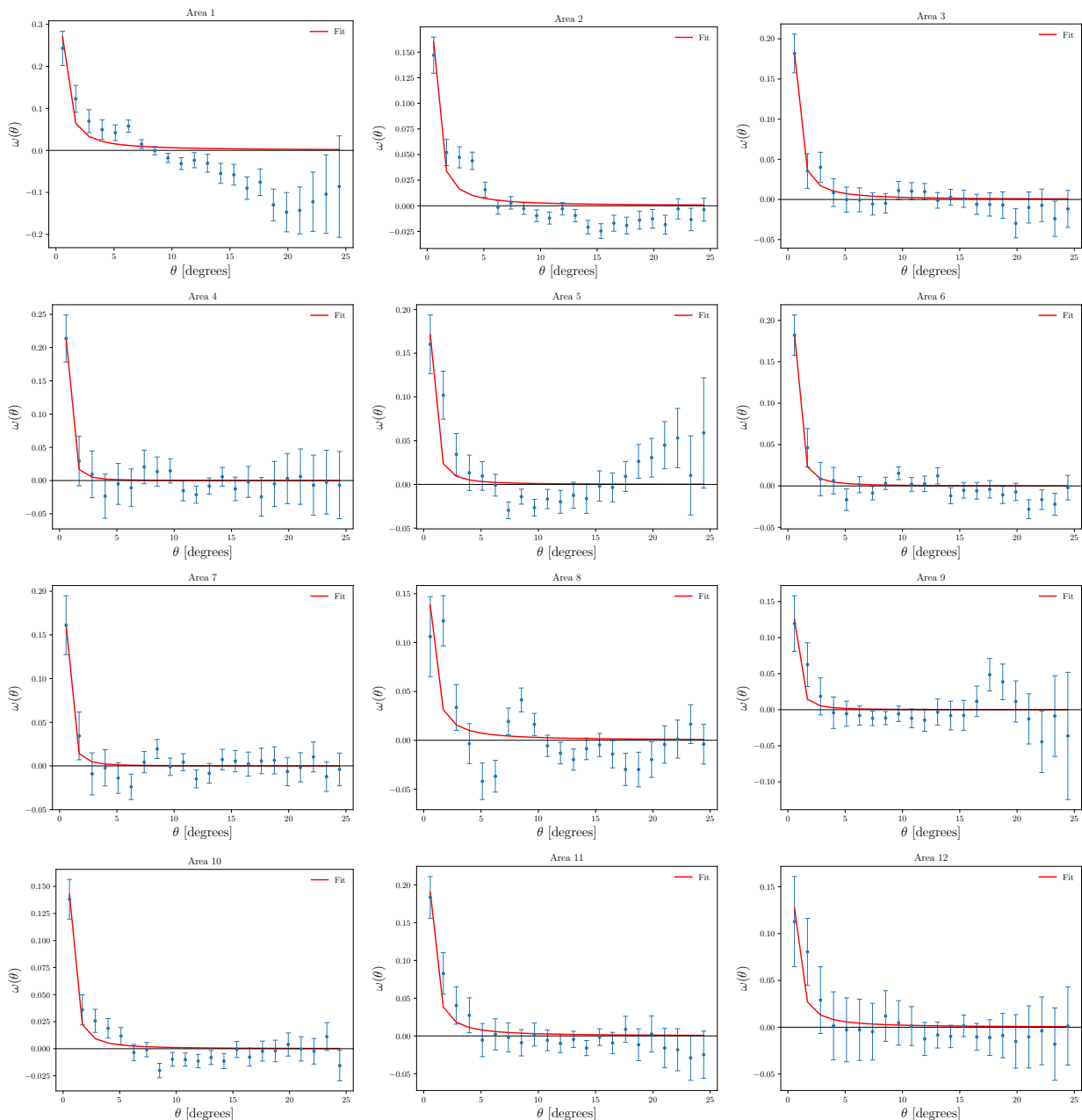


FIG. 8. 2PACF for large-angle analyses in Shell 2. Angular distribution of the 12 regions illustrated in Figure 3 within the angular range $0^\circ < \theta \leq 25^\circ$.

However, with the 2PACF at large scales we obtain even more information, since one can recognize the presence of large over-dense and/or under-dense cosmic structures in the Areas in study (see Sections IV B and IV B 1). These results enhance our understanding of the evolutionary processes that have shaped the large-scale structure of the Universe across cosmic time (Ando et al. 2018, Avila et al. 2021, Fang et al. 2020).

Our results with the 2PACF serve as a consistency test of the model, represented in the mocks, and at the same time they represent a directional analysis of the cosmic tracer displayed in the selected 12 Areas, confirming the

validity of the statistical isotropy in the Local Universe in each shell.

In our analyses of the angular power spectrum estimator, we inspect the two redshift shells and compare the results in the context of the Λ CDM model, comparing observational results with theoretical predictions. For multipoles $\ell \lesssim 90$, the observed power spectra for both shells show a bias close to 1, consistent with linear theory within a 2σ confidence interval. However, deviations from linear theory are observed for larger multipoles, particularly for Shell 1, which corresponds to the Local Universe. This suggests that local structures contribute significantly

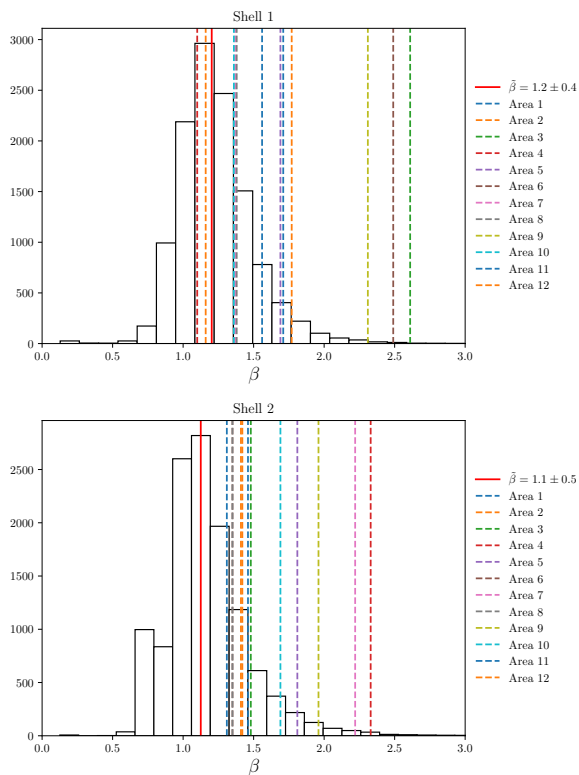


FIG. 9. Large-scales case. **Upper:** Distribution of the best-fit parameters of 1,000 Area-mocks in Shell 1 ($0 \leq z < 0.06$). The median and standard deviation are $\tilde{\beta} = 1.2 \pm 0.4$. **Bottom:** Distribution of the best-fit parameters of 1,000 Area-mocks in Shell 2 ($0.06 \leq z < 0.12$). The median and standard deviation are $\tilde{\beta} = 1.1 \pm 0.5$.

to non-linearities, with a notable increase in power at smaller scales. The comparison with log-normal simulations further confirms these effects, especially for Shell 1, where the disagreement between data and simulations is observed for the lower scales, that is, $\ell \gtrsim 90$.

Moreover, we also take advantage of the CDF tool which provides useful insights to the third dimension, the radial distances (they are calculated using cosmography and are given in units $\text{Mpc } h^{-1}$, where $H_0 \equiv 100 h \text{ km s}^{-1} \text{ Mpc}^{-1}$). By comparing the CDFs of a set of Areas both in Shell 1 and Shell 2, distinctive patterns emerge, namely regions revealing strong matter clustering followed by voids, a signature consistent across the Areas within the same shell, but showing a different pattern when comparing the same Area across the two shells. This, once more, reinforces the evolutionary differences, as Shell 1 corresponds to older structures than Shell 2. Moreover,

the CDF analysis reveals that these features, including the presence of voids and clusters, are independent of the number of galaxies in each Area. These findings complement our angular, or 2D, clustering studies.

Additionally, the maps presented in Figure 14 further illustrate the evolutionary disparity between the two redshift shells. While Shell 1 exhibits a more developed network of cosmic structures, Shell 2 reflects a younger epoch, where these cosmic structures are still in the process of formation. This strengthens the results observed in the angular and radial analyses, emphasizing the dynamic of structure formation. Furthermore, wedge plots complement the information provided by CDFs, giving light to understand the imprints left by cosmic structures in the results obtained with other tools; in summary, helping to unveil features partially or totally hidden in other examinations.

Finally, the number-count maps, displayed in Figure 14, illustrates well our conclusions, summarizing the results of our study. We performed analyses that were consistent with the Λ CDM model, separately, in each shell. But this consistency works just as a snapshot in each shell, however the Λ CDM model describes also the dynamics of the matter clustering evolution, and therefore it can also be tested in this regard. A comparison between shells of the clustering features, done with diverse estimators, should make such cosmic evolution evident. This is precisely what has been done in subsections IV A, IV B, and IV C, and is well illustrated in Figure 14: the older part of the Universe seen in Shell 1, $z \approx 0$, shows structures suggestive of filament-like morphology, where various large overdensities are present but also well-defined void structures are noticeable, instead such structures are not remarkable in the younger part of the Universe represented in Shell 2.

ACKNOWLEDGMENTS

CF and AB thank the Coordenação de Aperfeiçoamento de Pessoal de Nível Superior (CAPES) and Conselho Nacional de Desenvolvimento Científico e Tecnológico (CNPq) for their grants under which this work was carried out. FA thanks CNPq and Fundação Carlos Chagas Filho de Amparo à Pesquisa do Estado do Rio de Janeiro (FAPERJ), Processo SEI 260003/014913/2023 for financial support.

DATA AVAILABILITY

The data underlying this article will be shared on reasonable request to the corresponding author.

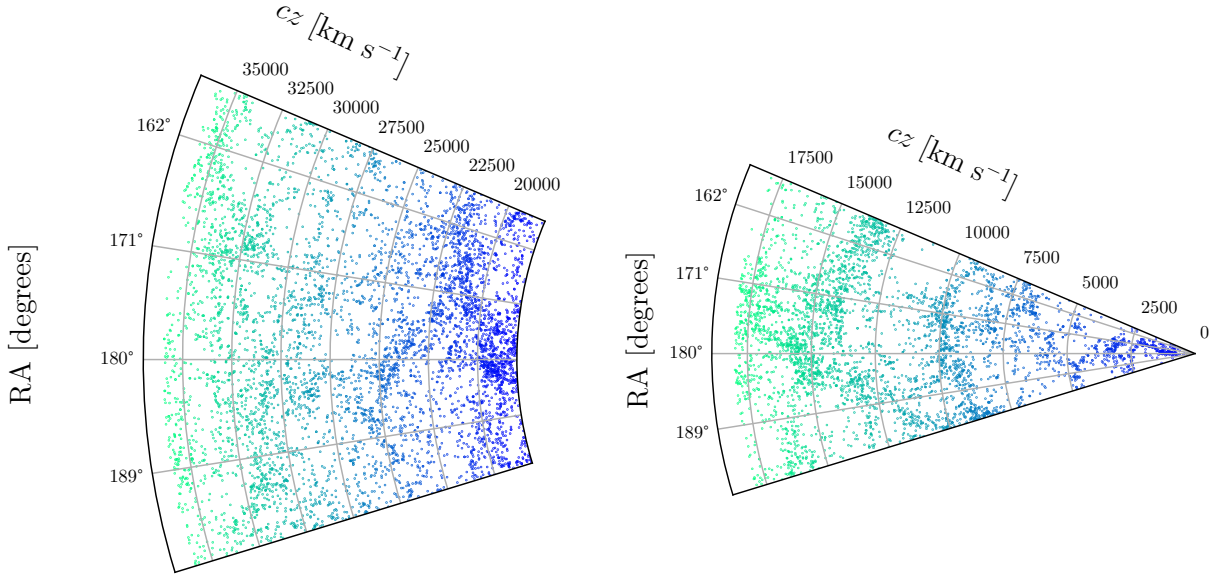


FIG. 10. Wedge plot of Area 5 from Shell 2 (left panel) and Shell 1 (right panel); these plots include physical distances of the blue galaxies to the origin, in units of km s^{-1} . We notice the presence of bulges of blue galaxies at several distances from the origin, data that appear as clustered matter when projected on the sky (i.e., Area 5).

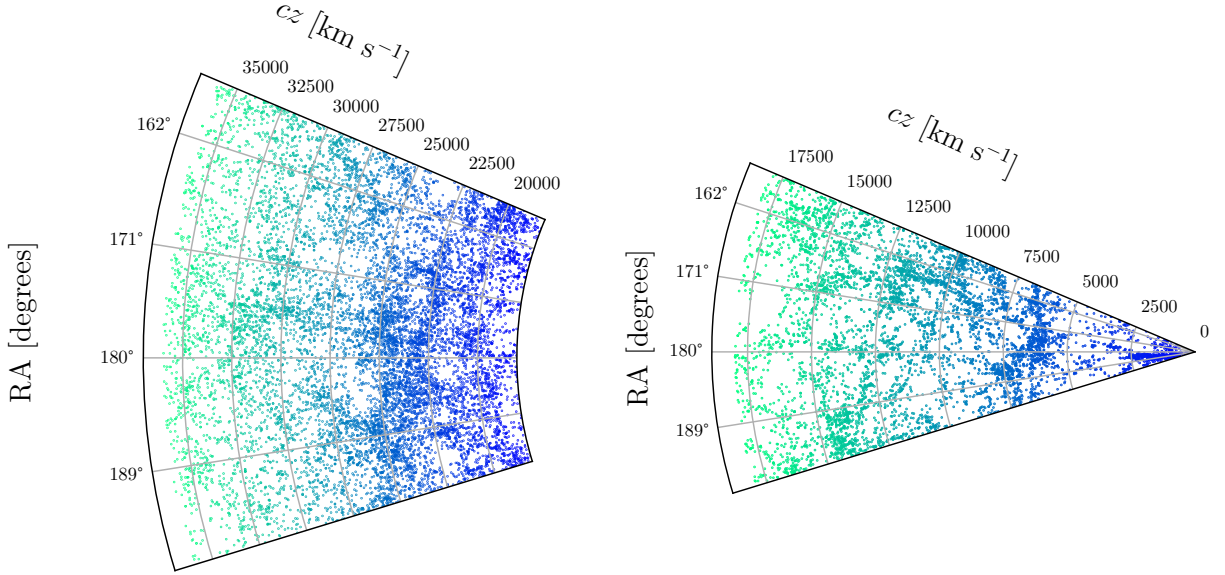


FIG. 11. Wedge plot of Area 8 from Shell 2 (left panel) and Shell 1 (right panel); these plots include physical distances of the blue galaxies to the origin, in units of km s^{-1} . We notice the presence of much more blue galaxies than in the wedge plot of Area 5 (see the Table I for the observational features of the 12 Areas in study). Again, large concentrations of galaxies are observed at several distances from the origin, data that also appear clustered when projected on the sky (i.e., Area 8).

Bellido J., Sánchez E., 2015, MNRAS, 449, 670
 Alonso D., Sanchez J., Slosar A., LSST Dark Energy Science Collaboration 2019, MNRAS, 484, 4127
 Ando S., Benoit-Lévy A., Komatsu E., 2018, MNRAS, 473, 4318
 Asorey J., Croce M., Gaztañaga E., Lewis A., 2012, MNRAS, 427, 1891

Avila F., Novaes C. P., Bernui A., de Carvalho E., 2018, J. Cosmology Astropart. Phys., 12, 041
 Avila F., Novaes C. P., Bernui A., de Carvalho E., Nogueira-Cavalcante J. P., 2019, MNRAS, 488, 1481
 Avila F., Bernui A., de Carvalho E., Novaes C. P., 2021, MNRAS, 505, 3404
 Avila F., de Carvalho E., Bernui A., Lima H., Nunes R. C.,

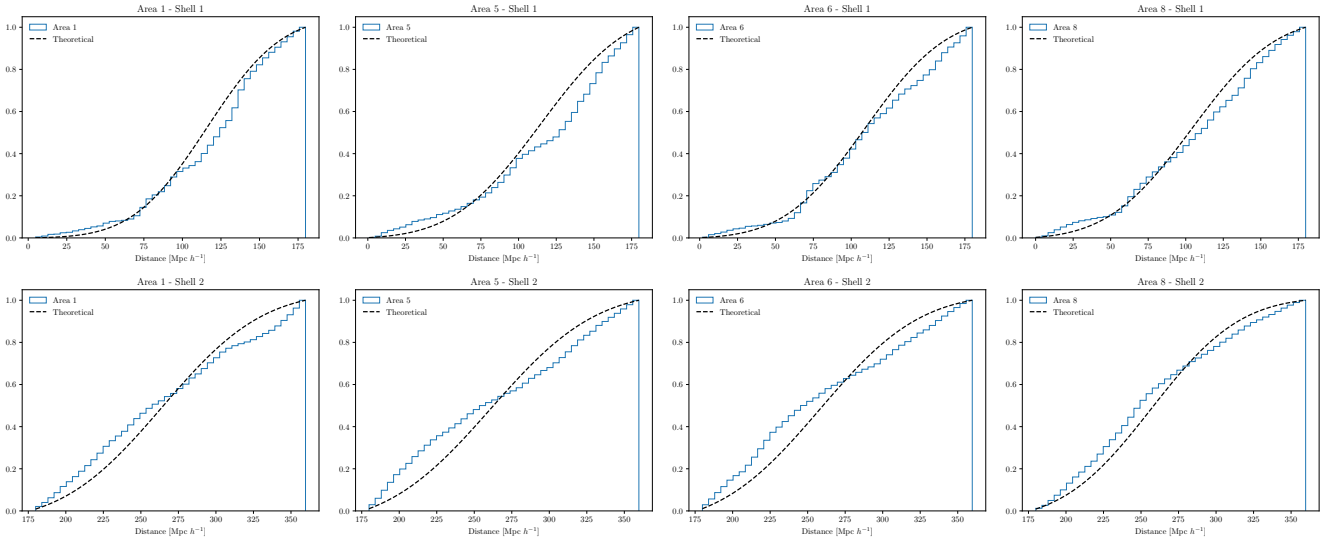


FIG. 12. The first (second) row shows the CDF analysis for the Areas 1, 5, 6, 8 from the Shell 1 (Shell 2). Differences among different Areas in each shell are noticed. But, Areas in a given shell, which means structures with the same age, notably follows the same pattern, namely regions of similar scales with strong clustering followed by regions with lack of galaxies (voids). All these features appear independent of the number galaxies in each Area, N_i , as can be corroborated in the Figures 10 and 11, which presents the wedge plots of Area 5 with $N_5 = 4, 292$ and $5, 921$, and Area 8 with $N_8 = 6, 170$ and $12, 144$, for Shell 1 and Shell 2, respectively (see Table I). Notice that the 2PACF of these four Areas show different signatures (see Figures 7 and 8).

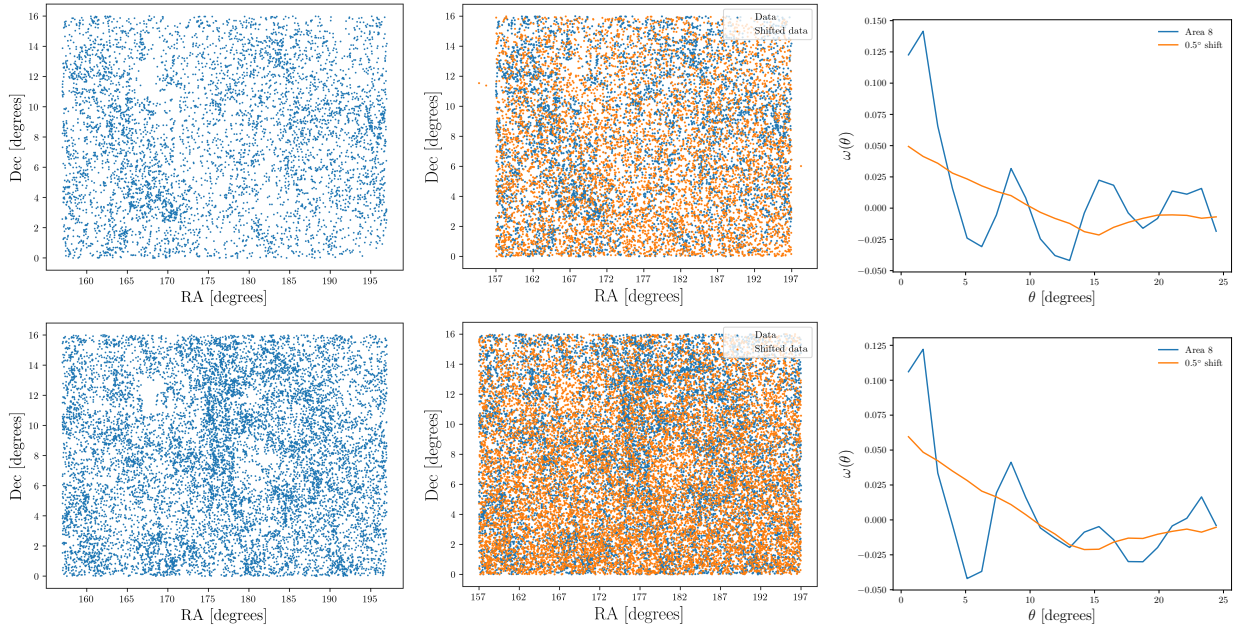


FIG. 13. Consistency analysis for the clustered structures mapped in Area 8. In both shells, the 2PACF from Area 8 reveals a set of lumps and valleys at diverse angular scales. If they correspond to galaxies concentrated in small groups or galaxy clusters then the shuffling of their angular positions will tend to destroy these features. **First row:** We display the Area 8 from Shell 1. The sequence of pictures, from left to right, is: (i) the original 2D blue galaxies distribution; (ii) these blue galaxies overlapped with their shuffled distribution (see the text for details); (iii) the 2PACF study for both distributions, i.e., analyses of the original distribution together with that one from the shuffled distribution. **Second row:** We display the Area 8 from Shell 2. The sequence of pictures follows the same procedures explained for the panels in the first row.

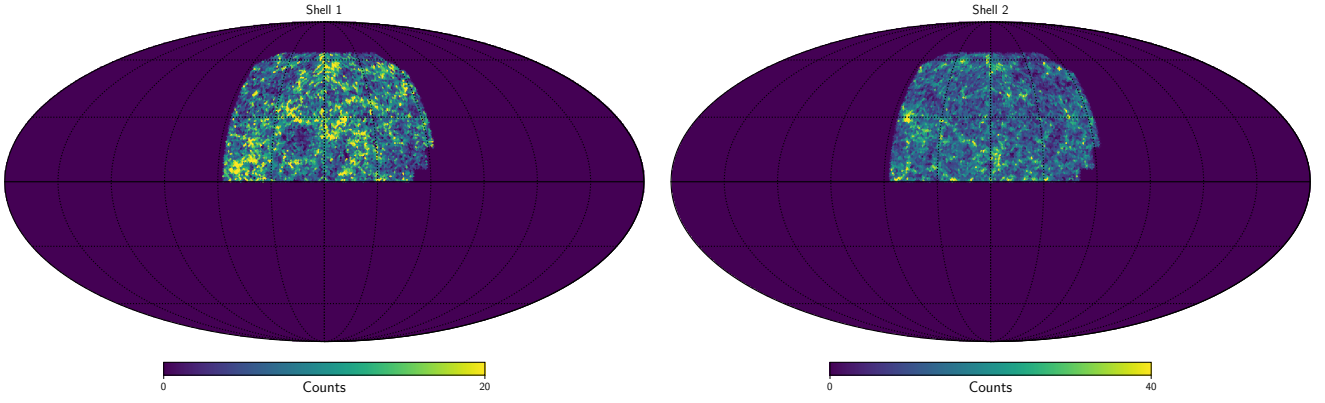


FIG. 14. Number-count maps of the SDSS blue galaxies, for Shell 1 (left map) and Shell 2 (right map), respectively. The maps were constructed using $N_{\text{side}} = 64$. A number-count map represents the pixelized distribution of galaxies in the footprint of the data in study, to facilitate the computation of its angular power spectrum. Notice that the older part of the Universe, displayed in Shell 1, $0 \leq z < 0.06$, exhibits a more developed network of cosmic structures: clustered matter, voids, and filaments, in comparison to the scenario observed in Shell 2, $0.06 \leq z < 0.12$, where matter appears more uniformly distributed.

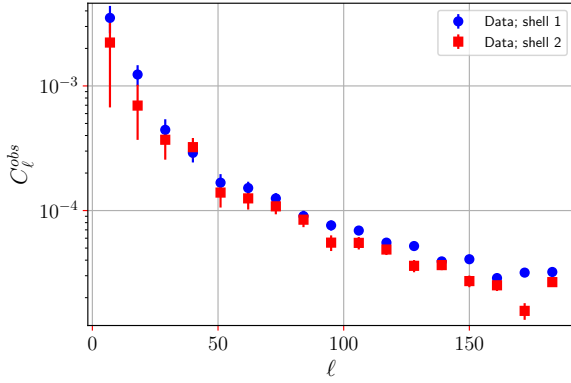


FIG. 15. True angular power spectrum, after shot-noise subtraction, for the two shells. The multipole range is $\ell \in [7, 183]$ with a bin size of $\Delta\ell = 11$. In this analysis, data from both shells show more power at small ℓ , which decreases at large ℓ . Additionally, at small scales, data from Shell 1 display slightly more power than data from Shell 2, while at large scales, the power spectra in both shells are comparable.

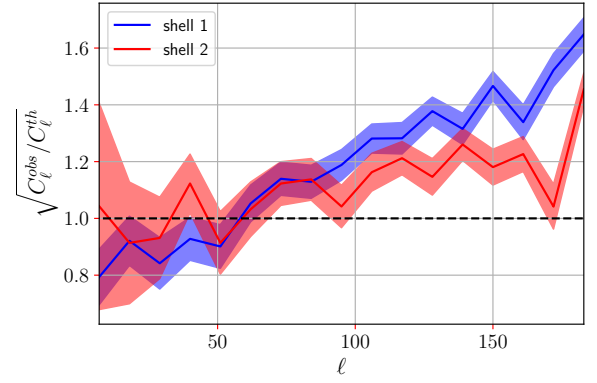


FIG. 16. Comparison of the observed and theoretical angular power spectra for both shells. The shaded region represents 1σ error. Up to $\ell \simeq 90$, both curves show a bias close to 1 within a 2σ confidence interval. For $\ell > 100$, non-linear effects become evident, with the observed spectra showing more power than expected from linear growth theory at small angular scales.

tic Astronomy and Cosmology. Springer, Dordrecht, p. 387, doi:10.1007/978-94-007-5609-0_8
 Coil A. L., 2013b, in Oswald T. D., Keel W. C., eds, , Vol. 6, Planets, Stars and Stellar Systems. Volume 6: Extragalactic Astronomy and Cosmology. Springer, p. 387, doi:10.1007/978-94-007-5609-0_8
 Coles P., Jones B., 1991, MNRAS, 248, 1
 Connolly A. J., et al., 2002, ApJ, 579, 42
 Courtois H. M., Hoffman Y., Tully R. B., Gottlöber S., 2012, ApJ, 744, 43
 Courtois H. M., Pomarède D., Tully R. B., Hoffman Y., Courtois D., 2013, AJ, 146, 69
 Courtois H. M., Mould J., Hollinger A. M., Dupuy A., Zhang C.-P., 2025, arXiv e-prints, p. arXiv:2502.01308
 Cybulski R., Yun M. S., Fazio G. G., Gutermuth R. A., 2014, MNRAS, 439, 3564

DESI Collaboration et al., 2024, arXiv e-prints, p. arXiv:2404.03000
 Davis M., Peebles P. J. E., 1983, apj, 267, 465
 Donoso E., Yan L., Stern D., Assef R. J., 2014, ApJ, 789, 44
 Dressler A., 1980, ApJ, 236, 351
 Einasto J., 2001, New A Rev., 45, 355
 Einasto M., et al., 2011, ApJ, 736, 51
 Fang X., Krause E., Eifler T., MacCrann N., 2020, J. Cosmology Astropart. Phys., 2020, 010
 Foreman-Mackey D., Hogg D. W., Lang D., Goodman J., 2013, PASP, 125, 306
 Franco C., Avila F., Bernui A., 2024, MNRAS, 527, 7400
 Franco C., Oliveira J., Lopes M., Avila F., Bernui A., 2025, MNRAS,
 Gavazzi G., Fumagalli M., Cucciati O., Boselli A., 2010, A&A, 517, A73
 Górski K. M., Hivon E., Banday A. J., Wandelt B. D., Hansen

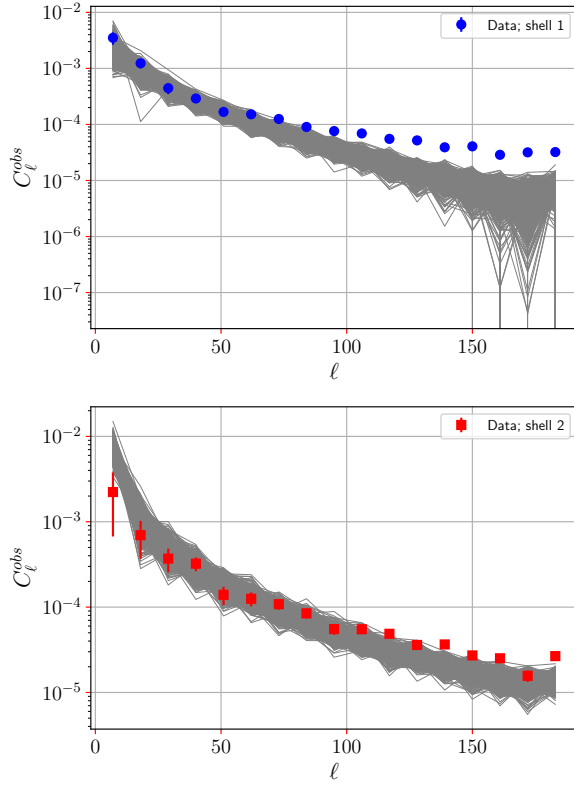


FIG. 17. Comparative study of the angular power spectra calculated from the data, in each shell, with respect to the spectra obtained from the analyses of the set of log-normal simulations (mock data). **Upper panel: Shell 1 analysis.** One observes that data and simulations agrees well until $\sim 2^\circ$, which corresponds to $\ell = 90$; for lower scales (i.e., larger ℓ) there is an increasing difference between both data because the non-linear growth of structures dominates. **Lower panel: Shell 2 analysis.** In this case, data and simulations agree well until $\sim 1^\circ$, corresponding to $\ell = 180$; notice that we are finding the same physical scale of non-linearity in both shells: $D_A^{\text{Shell 1}} \times 2^\circ \simeq D_A^{\text{Shell 2}} \times 1^\circ$, because the angular diameter distance to Shell 2 is, approximately, the double than the angular diameter distance to Shell 1.

F. K., Reinecke M., Bartelmann M., 2005, *ApJ*, 622, 759
 Gunn J. E., Gott III J. R., 1972, *ApJ*, 176, 1
 Hamilton A. J. S., 1993, *apj*, 417, 19
 Hewett P. C., 1982, *mnras*, 201, 867
 Hoffman Y., Pomarède D., Tully R. B., Courtois H. M., 2017, *Nature Astronomy*, 1, 0036
 Holm-Hansen C., Putman M. E., Kim D. A., 2025, *MNRAS*, 536, 3507
 Hoyle F., Vogeley M. S., Pan D., 2012, *MNRAS*, 426, 3041
 Jarvis M., 2015, *TreeCorr: Two-point correlation functions*, Astrophysics Source Code Library, record ascl:1508.007
 Keihänen E., et al., 2019, *A&A*, 631, A73
 Kitaura F.-S., Erdoğan P., Nuza S. E., Khalatyan A., Angulo R. E., Hoffman Y., Gottlöber S., 2012, *MNRAS*, 427, L35
 Kurki-Suonio H., 2023, *Galaxy Survey Cosmology*, <https://www.mv.helsinki.fi/home/hkurkisu/GSC1.pdf>
 Landy S. D., Szalay A. S., 1993, *apj*, 412, 64

Leistedt B., Peiris H. V., Mortlock D. J., Benoit-Lévy A., Pontzen A., 2013, *MNRAS*, 435, 1857
 Lopes M., Bernui A., Franco C., Avila F., 2024, *ApJ*, 967, 47
 Marques G. A., Bernui A., 2020, *J. Cosmology Astropart. Phys.*, 05, 052
 Matthewson W. L., Durrer R., 2022, *J. Cosmology Astropart. Phys.*, 2022, 035
 Mo H., van den Bosch F. C., White S., 2010, *Galaxy Formation and Evolution*. Cambridge University Press
 Novaes C. P., Bernui A., Xavier H. S., Marques G. A., 2018, *MNRAS*, 478, 3253
 Nuza S. E., Kitaura F.-S., Heß S., Libeskind N. I., Müller V., 2014, *MNRAS*, 445, 988
 Pan D. C., Vogeley M. S., Hoyle F., Choi Y.-Y., Park C., 2012, *MNRAS*, 421, 926
 Papovich C., 2008, *ApJ*, 676, 206
 Peebles P. J. E., 1980, *The large-scale structure of the universe*. Vol. 96, Princeton university press
 Peebles P. J. E., 1993, *Principles of Physical Cosmology*. Princeton University Press, doi:10.1515/9780691206721
 Peebles P. J. E., Hauser M. G., 1974, *apjs*, 28, 19
 Pillepich A., et al., 2018, *MNRAS*, 473, 4077
 Planck Collaboration et al., 2020, *A&A*, 641, A6
 Pomarède D., Courtois H., Tully R. B., 2013, in de Grijs R., ed., *IAU Symposium Vol. 289, Advancing the Physics of Cosmic Distances*. pp 323–326 (arXiv:1211.2915), doi:10.1017/S174392131202162X
 Postman M., Geller M. J., 1984, *ApJ*, 281, 95
 Press W. H., Schechter P., 1974, *ApJ*, 187, 425
 Ramella M., Geller M. J., Huchra J. P., 1992, *ApJ*, 384, 396
 Sarkar S., Pandey B., 2025, *J. Cosmology Astropart. Phys.*, 2025, 023
 Sawangwit U., Shanks T., Abdalla F. B., Cannon R. D., Croom S. M., Edge A. C., Ross N. P., Wake D. A., 2011, *MNRAS*, 416, 3033
 Schaye J., et al., 2015, *MNRAS*, 446, 521
 Schneider P., 2006, *Extragalactic Astronomy and Cosmology*. Springer
 Sheth R. K., van de Weygaert R., 2004, *MNRAS*, 350, 517
 Sousbie T., 2011, *MNRAS*, 414, 350
 Springel V., et al., 2005, *Nature*, 435, 629
 Strateva I., et al., 2001, *AJ*, 122, 1861
 Tegmark M., et al., 2002, *ApJ*, 571, 191
 Thomas S. A., Abdalla F. B., Lahav O., 2011, *MNRAS*, 412, 1669
 Totsuji H., Kihara T., 1969, *PASJ*, 21, 221
 Trotta R., 2017, arXiv e-prints, p. arXiv:1701.01467
 Tully R. B., Shaya E. J., Karachentsev I. D., Courtois H. M., Kocevski D. D., Rizzi L., Peel A., 2008, *ApJ*, 676, 184
 Valade A., Libeskind N. I., Pomarède D., Tully R. B., Hoffman Y., Pfeifer S., Kourkchi E., 2024, *Nature Astronomy*, 8, 1610
 Wang Y., Brunner R. J., Dolence J. C., 2013, *MNRAS*, 432, 1961
 White S. D. M., Frenk C. S., 1991, *ApJ*, 379, 52
 Wu Y.-W., Xia J.-Q., 2025, *The Astrophysical Journal*, 979, 3
 York D. G., et al., 2000, *AJ*, 120, 1579
 Zonca A., Singer L., Lenz D., Reinecke M., Rosset C., Hivon E., Gorski K., 2019, *Journal of Open Source Software*, 4, 1298
 de Carvalho E., Bernui A., Carvalho G. C., Novaes C. P., Xavier H. S., 2018, *J. Cosmology Astropart. Phys.*, 04, 064

Appendix A: Robustness of Angular Power Spectrum Results with Varying Resolution

To assess the robustness of the result obtained with $N_{\text{side}} = 64$, we present the angular power spectrum for $N_{\text{side}} = 32$. Figure 18 compares the C_ℓ measurements for both shells between $N_{\text{side}} = 32$ and $N_{\text{side}} = 64$. Note that the results are shown up to $\ell = 84$ due to the resolution loss in the pixels with the decrease in N_{side} . Overall, there are no significant variations in the C_ℓ measurements for both shells when reducing the map resolution, which strengthens the results and their interpretation presented in Section IV C.

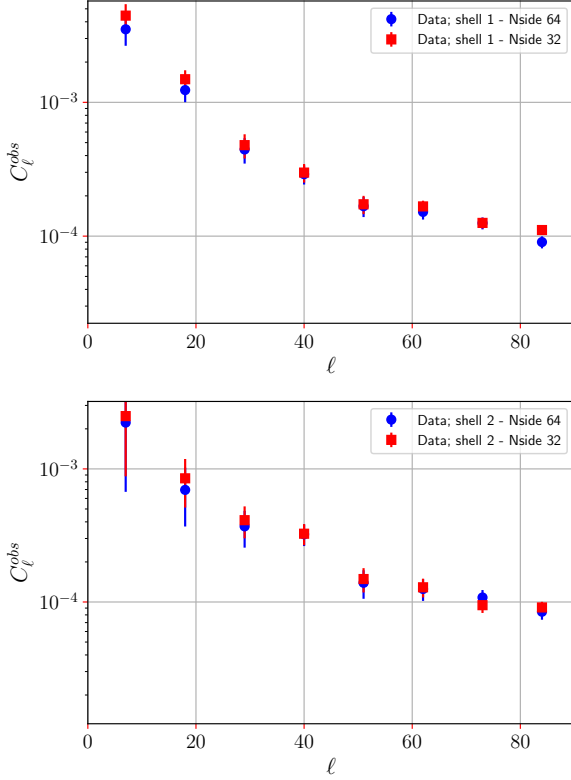


FIG. 18. Consistency test for different angular resolutions. We compute the angular power spectra, C_ℓ , from data in the two shells to verify the consistency of our results when considering two angular resolutions, namely, $N_{\text{side}} = 32$ and $N_{\text{side}} = 64$. In both plots, our results are presented up to the common multipole $\ell = 84$, due to their different limit resolutions. As observed, there is no significant difference in the results obtained in both cases.